Chapter 2
Processing and Assembly

The Role of a Heat Affected Zone (HAZ) on Mechanical Properties in Thermally Welded Low Density Polyethylene Blown Film

Timothy E. Weston
Pennsylvania College of Technology, USA
Ian R. Harrison
Pennsylvania State University, USA

INTRODUCTION

Low density polyethylene (LDPE) thin films are produced by blown film extrusion. In practice, the lay-flat produced during this process is slit to thin film or used in tubular fashion to produce products such as bags. In either case, it is common to thermally weld these films during the manufacturing process. The properties of the products produced depend on the strength of the film as extruded as well as the strength of the thermal weld used to join pieces of film together. One important property in LDPE film applications is cold service temperature. As the service temperature for LDPE is lowered, the material and film undergo a ductile to brittle transition. Film properties on the brittle side of this transition exhibit significantly lower deformation to failure than is exhibited in ductile film. This lower observed ultimate deformation lowers impact properties and other properties related to ultimate deformation and the drawing process such as toughness. Thermal welding affects the low temperature utility of these thin films by shifting the ductile/brittle transition temperature for the film and weld system to higher temperatures than the film without welds. Therefore, as the cold service temperature increases, the ductile to brittle transition temperature is encountered closer to ambient temperature, thus reducing the low temperature performance of welded film. It has been suggested in the literature that this shift in low temperature utility arises from a geometric concentration of stress at the weld - film interface.[1]

Other literature sources report changed mechanical properties in a well-characterized area termed the heat affected zone (HAZ). The HAZ is defined as unmelted but changed material directly adjacent to a thermal weld. The reports of a HAZ are limited to the joining of larger parts. These larger parts were welded by other welding techniques such as butt or hot plate welding. Several key differences exist between the large parts studied and the results reported here. Clearly, in previous works parts are more massive and the weld times observed are significantly longer than weld times in thin film welds. Larger parts cool more slowly and retain the weld energy longer than a thin film. Therefore, the development of a HAZ in large parts is a function of thermal transport over much longer heating times. Thin film welding times are much shorter, typically 2-3 seconds versus minutes for large parts, and therefore the presence of a HAZ may not be a significant factor in the performance of thin film welds. A HAZ analogous to those observed in thick parts has never been reported in the case of thin film welds.

The problem is then:

(1) to determine if there exists a HAZ present in thermally welded LDPE thin film.

(2) to determine whether this HAZ has different properties than the original blown film.

(3) to determine if the shift in low temperature ductile/brittle failures are caused by geometric stress concentration or the presence of a HAZ weaker than either the original blown film or the thermal weld.

EXPERIMENTAL

EXPERIMENTAL OVERVIEW

Three experiments were performed in order to confirm the role of a Heat Affected Zone (HAZ) in the low temperature performance of LDPE thin films. Low temperature mechanical testing was used to determine the correlation between weld temperature and change in ductile/brittle service temperature. Optical microscopy was used to detect the presence of a HAZ and also to determine any correlation between size of the HAZ and welding temperature. Finally, Small Angle X-Ray Scattering (SAXS) was used to determine if the optical observation of a HAZ was related to a measurable structural or morphological difference between the HAZ, weld, and parent film. Welded samples were prepared using a Doboy Model HS-C continuous thermal welder (Doboy Packaging Machinery, Inc. New Richmond WI) traveling at 20 feet/min. Figure 1 is an illustration of this welder. Two film materials, Winzen Stratofilm and Raven Astrofilm, were provided in 6 foot wide rolls of lay flat. The first material was produced by Winzen International,

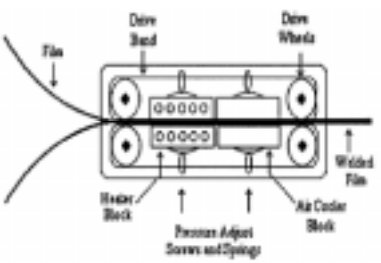

Figure 1. Doboy thermal welder.

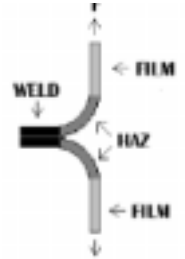

Figure 2. Position of the HAZ in thermal welds.

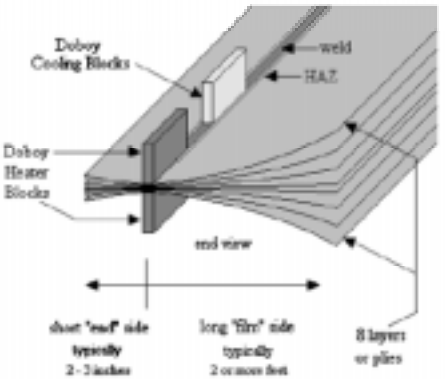

Figure 3. Film welding showing the 8-ply arrangement.

Inc. San Antonio, Texas designated Stratofilm 372, roll # 40949120 with nominal 0.8 mil film thickness. This material was selected because of failed welds during high altitude flights in the NASA scientific balloon program. This film has been a balloon industry benchmark as early as 1974. Samples were welded longitudinally in eight layers simulating high altitude balloon cap production. Figures 2 and 3 illustrate of this arrangement. Welding temperature was varied to produce five test groups representing weld temperatures of 100, 125, 150, 175, and 200^{O}C. Welding pressure was controlled using adjustment screws on the Doboy welder in series with leaf style springs.

MECHANICAL TESTING

Mechanical testing was performed using an Instron 4200 tensile testing system equipped with a Series IX Automated Materials Testing System v6.02 data analysis package. A low temperature chamber was available for the low temperature experiments described below. Samples were divided into one inch wide specimens three inches in length using a sharp razor blade. Specimens that did not cut cleanly on the first try were discarded as potentially problematic due to the presence of notches. All samples were trimmed to provide an overall length of three inches. Both room temperature and low temperature mechanical tests were performed in accordance with ASTM Method D882 “Standard Test Methods for Tensile Properties of Thin Plastic Sheeting”. Strain rate for room temperature experiments was 508 mm/min (20 in/min). For both film and weld samples, an initial distance between the grip of 50.8 mm (2 inches) was employed. All samples were tested in replicates of five samples per condition. Low temperature specimens were allowed to equilibrate for a minimum of 45 minutes at test temperature. This sample conditioning is similar to those found in other works.[1]

OPTICAL MICROSCOPY

Different regions in welded LDPE thin film can be seen with the naked eye. In contrast, LDPE film is commonly translucent and very uniform in appearance. In welded film, the weld area is much more transparent than the parent film and contains minor visual inconsistencies. While not immediately obvious, there exists a region between the film and weld that is clearly not like either the parent film or the weld area. This region is small, on the order of several (2-3) mm in width, but is easily identified with the naked eye. The purpose of this experiment was to use optical microscopy to help understand the size and nature of this zone found between the weld and the parent film. For this experiment two optical microscopes were used. An Olympus SZH-ILLB stereoscope was used for low power observations, and an Olympus BH-2 microscope was used for higher power observations. The Olympus BH-2 microscope was equipped with crossed polarizers used to increase contrast in stressed samples. Both microscopes were compatible with an Olympus Model PM 10 AD Photomicrographic system. Both systems were also compatible with a Javelin MTV-3 video camera attachment.

SMALL ANGLE X-RAY SCATTERING (SAXS)

The equipment used for the SAXS experiment was a Siemens FK-60 Cu X-ray tube operating on a Siemans Kristaloflex K710 generator. X-rays were pinhole collimated using three successive pinholes to reduce parasitic scatter. The X-ray detector used was a STAR-1 computer integrated system, manufactured by Photometrics Ltd. This system uses a CCD (charge coupled device) for X-ray detection. The STAR-1 data acquisition system is comprised of a control, interface, and instruments units. The STAR-1 was connected, using a IEEE-488 interface, to a Macintosh IIci computer. Dark current (noise) measurements were collected and computer subtracted from the scattering data. A commercial software package, IP Lab-PMI, was used to manipulate the scattering data to intensity plots or color enhanced images.

RESULTS AND DISCUSSION

MECHANICAL TESTING

Samples from the Winzen Stratofilm 372 were welded at 100, 125, 150, 175, and 200^{O}C. The parent film was tested as a control. The results are also graphically illustrated in Figure 4. Welding at temperatures of 125^{O}C or greater produced welds that varied by less than 2% in both stress at yield and 6% in % strain at break. Samples with welds produced at 100^{O}C failed at much lower yield stress and % strain at break. The 100^{O}C welded samples were observed to undergo failure in the weld region. The failure mode is commonly known as a

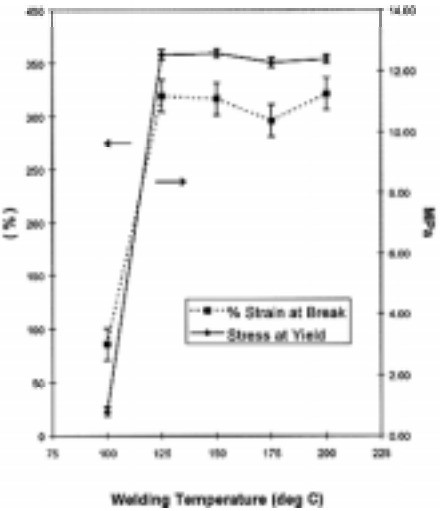

Figure 4. Room temperature stress and strain.

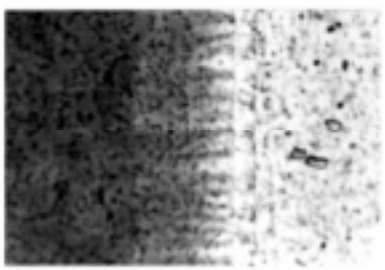

Figure 6. 7.5x Microphotograph of W200 welded LDPE film.

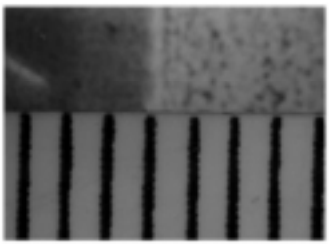

Figure 5. 7.5x Microphotograph of W200 welded LDPE film w/rule.

"peel seal". All other welded samples failed in a ductile fashion with deformation occurring throughout the length of the samples. The actual location of failure was random throughout the sample and did not occur at the weld. The parent film also exhibited ductile failure with significant strain prior to break. The stress at break value for the film was very much in line with the values observed with the welded samples. This increase can be attributed to the weld not participating in the strain of the sample because of a thickness roughly twice the film section thickness. All film and all welded samples failed at approximately 300% strain during ambient temperature testing. In contrast, all welded samples failed at approximately 20% strain or less at -80^{O}C. The brittle failures at -80^{O}C all occurred in the parent film parallel with and directly adjacent to the weld.

The parent film failed in both ductile and brittle modes at -80^{O}C. Stress at break values were comparable for both ductile and brittle failures at all three test temperatures. As expected, the stress at break values did increase with decreasing temperature. The test condition of most interest is -60^{O}C. At this temperature, there is a clear correlation between the number of samples exhibiting ductile failures and the welding temperature.

OPTICAL MICROSCOPY

Optical microscopy was used to observe and document the existence of a well-defined HAZ in samples welded from Winzen Stratofilm 372. Figure 5 is a microphotograph of the W200 welded film sample under combination front lighting and back lighting. The rule shown at the bottom of this microphotograph suggests the size of the HAZ as observed by low power microscopy to be on the order of 1.5 -3 mm. Figure 6 is a microphotograph of sample W200

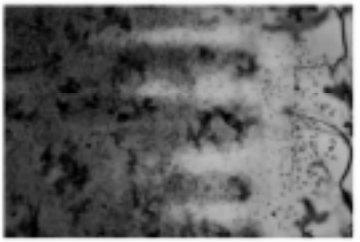

Figure 7. 15x Microphotograph of W200 welded LDPE film.

under 7.5x magnification. The weld is the light streak running vertically across the microphotograph. This microphotograph was lit to emphasize the film side of the weld. The film side of the weld is seen in the center to upper portion of the microphotograph. The terminal side of the weld is seen in the lower portion of the microphotograph. The parent film is seen in the top of the microphotograph. From this figure it is possible to observe the darker, more opaque nature of the film, the lighter, more translucent nature of the welded material, and the brown region in between the weld and the film. This brown region corresponds to the predicted position of a HAZ. It should be noted as well that while we struggled to document this obvious transition area using microphotography, it is easily visible to the naked eye, and the lighting necessary to produce a suitable photograph detracts from the ease of identifying this region. Figure 7 is a 15x magnification microphotograph of this same region. In this figure, the weld runs vertically across the microphotograph. The parent film is located to the left of the microphotograph. The HAZ can be observed in the center of the microphotograph between the film and weld. This microphotograph suggests there may be more than simple structure to the HAZ. One pattern common to much of the HAZ region is the finger like pattern caused by alternation of light and dark areas on the microphotographs. These “fingers” seem to form in the HAZ at the weld/HAZ interface. The finger like structures are often large enough to be easily seen using the naked eye. While this structure is very obvious, their cause is not. Possible causes include microscopic thickness variations, variations in crystallinity, or melt dynamics associated with the welding process occurring at 20 feet/min. It would be necessary to design a study to control these variables to determine the reproducibility and source of the “finger” structures.

SMALL ANGLE X-RAY SCATTERING (SAXS)

A series of SAXS experiments were designed in an effort to confirm structural differences between the weld, HAZ, and parent LDPE film. Because of the weak scattering nature of LDPE and the film thickness the data was collected from stacked samples. Data from several different stacking experiments did show approximately a 10Å difference between the weld region and HAZ. The corresponding difference in Plot Meridian FWHM is 0.2–0.3 mrad. This data reinforces the hypothesis that there are structural differences underlying the optical observations discussed previously.

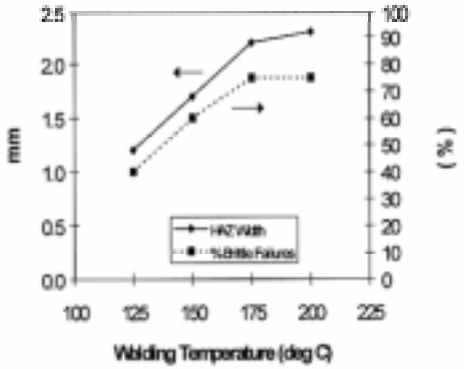

Figure 8. Brittle Failure Rate (-60ºC) and HAZ width vs. weld temperature

CONCLUSIONS

The optical microphotographs presented provide strong visual evidence for the existence of a HAZ in these welded LDPE thin films. The literature revealed that private sector companies had visually observed a HAZ in these LDPE films but did not realize the relevance of their observations. Our measurements of the observed HAZ scaled directly to the increase in heat input to the weld as measured by welding temperature. This observation is consistent with known models for thermal conductivity and literature reports of HAZ behavior.

Mechanical data presented provides strong evidence of affected mechanical properties in the welded LDPE thin film. In particular, the low temperature performance of the welded film system is compromised by a shift in the temperature where ductile to brittle transition occurs in the mechanical properties. The data presented clearly demonstrates the weld region would be expected to fail long before the surrounding parent film.

Finally, a correlation has been established between the increase in brittle failures and the width of the HAZ as observed by optical microscopy. Figure 8 clearly indicates this relationship. The graph in Figure 8 also demonstrates the dependence of the HAZ width and the rate of brittle failures with welding temperature. If geometry of the samples caused the failures, as observed by Simpson and Bowman, there would be no change in brittle failures with weld temperature. The increase in both HAZ width and brittle failure rate with increasing temperature suggests the increasing size of the HAZ is the key factor in the increased brittle failures seen in the welded LDPE thin film system studied here.

Future work on this research will seek to more accurately establish the nature of the structure, morphology, and extent of this HAZ and then tie these structural observations to possible causes in shifts in cold brittleness temperature. Ultimately, a model for predicting the generation of a HAZ and its affect on properties such as cold brittleness will be developed.

REFERENCES

1 Simpson, M., Bowman, *J, Polymer Engineering and Scienc*e, 31:7, 487 (1991)
2 Simpson, D.M., Harrison, I.R., ANTEC ‘93, 1206, (1993)
3 Winzen International, Winzen International, Inc. (1985)
4 Winzen International*, Winzen International, In*c. (1994)

5 Weisman, D. and Alexander, H., *Intern. J. Polymeric Mater.*, **3**:33 (1974)
6 Nieh, J.Y., and Lee, L.J., ANTEC ‘ 93, 388 (1993)
7 Stevens, S.M., ANTEC ‘96, 1275, (1996)
8 Stevens, S.M., ANTEC ‘94, 1258, (1994)
9 Jang, B.Z., Uhlmann, D.R., Vander Sande, J.B., *Journal of Applied Polymer Scienc*e, 29, 3409 (1984)
10 Gupta, A., Simpson, D.M., and Harrison I.R., ANTEC ‘93, 1201, (1993)

Effects of Processing Conditions on the Failure Mode of an Aliphatic Polyketone Terpolymer

Nicole R. Karttunen and Alan J. Lesser
Polymer Science and Engineering Department, University of Massachusetts, Amherst, Massachusetts 01003, USA

INTRODUCTION

It is well known that processing conditions can play a significant role in the physical and mechanical behavior of polymeric materials. Conditions such as process temperature, cooling rate and shear rate can have significant impact on the properties of the final product. The levels of orientation, residual stress, crystallinity, etc. are a few examples of characteristics that may be altered by varying such conditions during processing. These, in turn, affect the behavior of the material. This investigation reports the effects of shear rate and cooling rate on the failure mode of extruded tubes. The material studied is a semi-crystalline aliphatic polyketone terpolymer.

EXPERIMENTAL

MATERIAL AND SPECIMEN PREPARATION

Material was supplied by Shell Chemical Company. The aliphatic polyketone consists of perfectly alternating units of carbon monoxide and ethylene, with a small portion (approximately 6 mol percent) of ethylene units substituted with propylene units:

$$-(CO-CH_2CH_2)_m-(CO-CHCH_3)_n-$$

Properties of this material have been examined in many studies.[1-4]

Material was provided in the form of extruded pipe. Five samples were produced by processing at different extrusion conditions. The chosen conditions represent the range of practical processing conditions, and therefore a range of morphologies that is most likely to be created in actual products. As a reference, an “original morphology” (OM) was produced at standard extrusion conditions. The thermal history was altered for two additional samples. These were either cooled slowly (AM-“annealed morphology”) or rapidly (QM-“quenched morphology”) from the melt. The extrusion rate was altered for two additional samples, representing the highest and lowest practical shear rates. These samples are referred to as “rate 1” (R1) and “rate 2” (R2), however, the corresponding extrusion rates

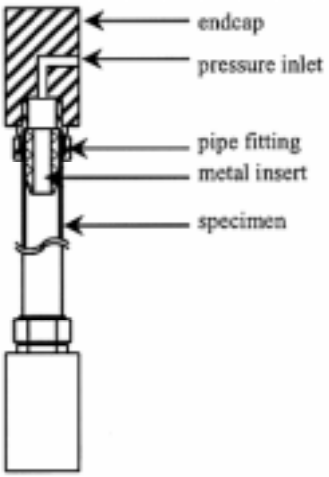

Figure 1. Schematic of biaxial testing specimen.

are not available from the supplier. As a note, the samples are labeled as different "morphologies", however, a priori, the actual morphologies of the samples were not known to be different. Rather, it is the possible similarities and differences in morphology that were to be determined and used as a "link" between the processing conditions and failure response.

The diameter of the specimens was approximately 22 mm with a wall thickness of 2 mm. The length was 15 cm. At each end, the cylinders were sealed with compression fittings and secured to a pipe fitting, which was threaded into steel cylinders. These cylinders were gripped in an Instron tension-torsion machine. A tap in the upper steel cylinder allowed internal pressurization with nitrogen gas. A schematic is shown in Figure 1.

MULTIAXIAL TESTING PROCEDURE

The testing procedure has been described in detail elsewhere,[5] and will only be discussed briefly here. The hollow cylindrical specimens were subjected to uniaxial and biaxial states of stress at 20°C at a nominal octahedral shear strain rate, of 0.05 min^{-1}. Tests were performed in an Instron 1321 tension-torsion machine modified with a Tescom ER3000 pressure regulator. The ratio of axial load to internal pressure was held constant for each test. Different stress states were applied to specimens by changing the value of this ratio. Each of the stress states within a given yield locus was applied at the same nominal octahedral shear strain rate. This was chosen as the method of control in order to be consistent with viscoelastic theory.

CRYSTALLINE PHASE

Crystallinity measurements were made by differential scanning calorimetry as well as by density gradient column. Calorimetry was performed on a Du Pont DSC 2910 at a heating rate of 10^{o}C/min. The values for the crystalline and amorphous phase densities used in crystallinity calculations were taken from.[6]

Crystalline orientation was determined by wide-angle x-ray diffraction, using pin-hole collimated, monochromated CuKα radiation. Patterns were collected on a GADDS detection system (Brucker).

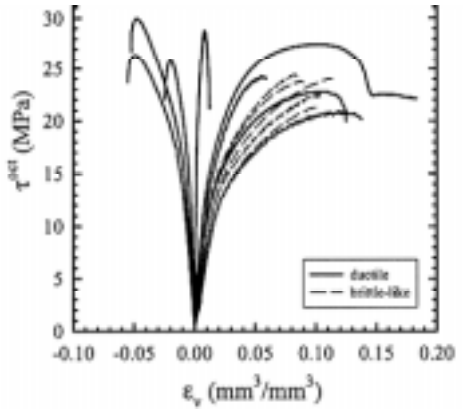

Figure 2. Plot of octahedral shear stress as a function of volumetric strain for the original morphology sample. Solid and dashed lines represent ductile and brittle-like behavior, respectively.

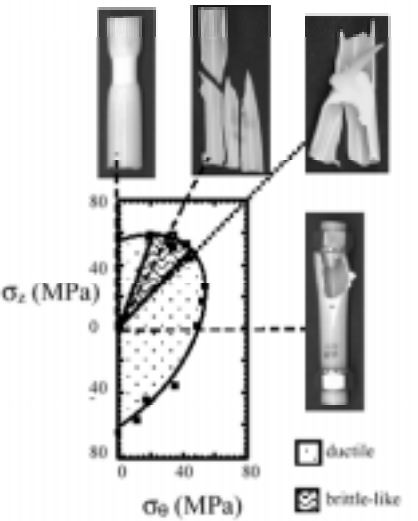

Figure 3. Representation of the ductile-brittle/transition for the original morphology sample. Dashed lines represent the stress state for the corresponding images. The dotted line indicates the case of equibiaxial tension.

RESIDUAL STRESS MEASUREMENT

Residual stresses may be induced during processing due to the inability of the material to contract upon cooling. Such stresses have been shown to affect the material behavior.[7-8] To determine if residual stresses were a factor in this behavior of this material, measurements were made using a procedure described by Clutton and Williams.[9] In this procedure, sections of tube are cut to various lengths and "strips" of material are removed from each section. By measuring the amount of ring closure or opening, the residual stress may be determined.

DISCUSSION OF RESULTS

FAILURE BEHAVIOR

The original morphology sample was used as a "reference" for comparison of the other samples. From a plot of the octahedral shear stress as a function of the volumetric strain for this sample, Figure 2, it is observed that several stress states result in a ductile-type response (the criteria used to determine ductile behavior is achievement of a zero-slope condition in this type of stress-strain curve). However, while it would be expected that the largest volumetrically straining stress states would be most likely to produce brittle response, this is not observed for this material. Some of the macroscopic failures for the original morphology are displayed in Figure 3.

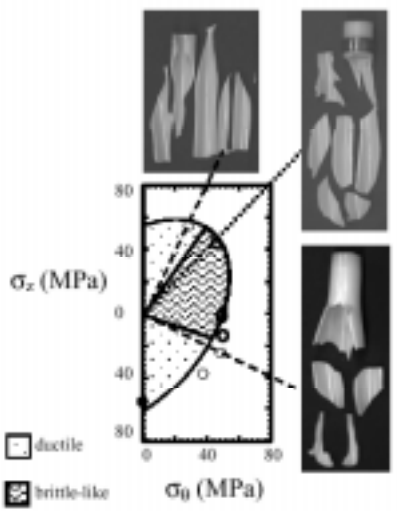

Figure 4. Representation of the ductile-brittle/transition for the annealed morphology sample. Dashed lines represent the stress state for the corresponding images. The dotted line indicates the case of equibiaxial tension.

Table 1. Crystallinity and melt temperature values determined by DSC and density gradient column

	Crystallinity by DSC, %	T_m, ^oC	Crystallinity by column, %
Original	34	225	34
Annealed	33	223	34
Quenched	33	223	34
Rate 1	33	224	35
Rate 2	35	224	36

The cooling rate had significant effect on the material behavior. Macroscopically, the failures of the quenched morphology sample appeared more brittle in nature than the original morphology. However, by the criteria described previously, in most stress states, ductile yield was achieved. In contrast, the annealed morphology was quite a bit more brittle in failure than the original morphology or the quenched morphology. In fact, the annealed morphology was the only sample for which a brittle type of response was observed for the case of equibiaxial tension, Figure 4. From this figure, it can be seen that the brittle-like regime for this sample was considerably larger than the other samples.

The extrusion rate seemed to be inconsequential to the failure behavior. The sizes of the ductile and brittle-like regimes for these two extrusion rates were similar to the original morphology. Again, ductile-types of failures were observed for the case of equibiaxial tension.

EFFECTS ON CRYSTALLINE COMPONENT

It appears as though the crystalline component was relatively unaffected by the different processing conditions. Table 1 presents the crystallinity as determined by DSC and by density gradient column, with no considerable differences between the samples. It in known that the crystallization kinetics of this polymer are very rapid,[10] and therefore significant changes in the crystallinity were not expected. Additionally, none of the samples exhibited

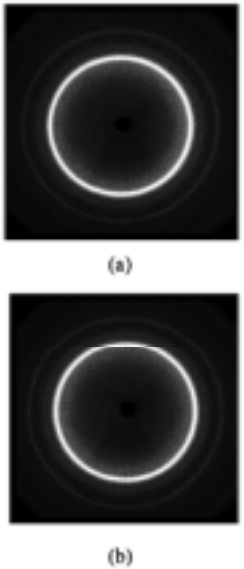

Figure 5. Sample WAXD patterns for polyketone terpolymer hollow cylinders: (a) original morphology, (b) annealed morphology.

Table 2. Residual stress values calculated for each sample.

	Residual hoop stress, MPa	Residual axial stress, MPa
Original	15.7	1.7
Annealed	16.8	0.6
Quenched	18.6	0.8
Rate 1	16.9	0.2
Rate 2	16.5	0.5

orientation in the crystalline phase (e.g., Figure 5). Similar patterns were observed for all samples. As a note, is it acknowledged that other differences may exist in the crystalline phase, for example, crystallite size. However, as a "rough" comparison of the apparent crystallite size, half-peak widths of the WAXD patterns were determined and found to be similar in all cases.

While there were no observed differences between the crystalline components of the samples, it is noted that this material is approximately 65% amorphous. Therefore, any effects on the amorphous component may have considerable effect on the behavior of this material. This is the topic of future work.

RESIDUAL STRESS

The amount of residual stress calculated for each sample is presented in Table 2. The stress in the hoop direction is considerably greater than that in the axial direction. Due to the presence of these stresses, the stress state that was applied to the specimens during testing was not equal to the actual stress state on the specimen. Rather, the applied stress was superimposed upon the existing residual stress. The original yield loci for the samples are presented in Figure 6 as axial stress vs. hoop stress. However, the presence of residual stress effectively shifts the yield loci in Figure 6 to that shown in Figure 7. In this figure, it can be seen that the brittle failures now fall in line with the case of equibiaxial tension. Thus, by considering the level of residual stress pre-existing in the specimens, we can account for the observation of ductile response in the stress state for which a brittle failure was expected.

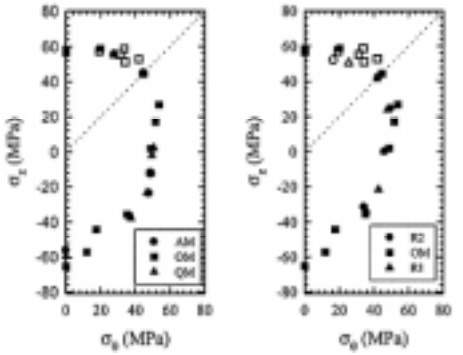

Figure 6. Yield loci for the various samples. Dashed line indicates equibiaxial loading. Solid and hollow symbols represent ductile and brittle-type failures, respectively.

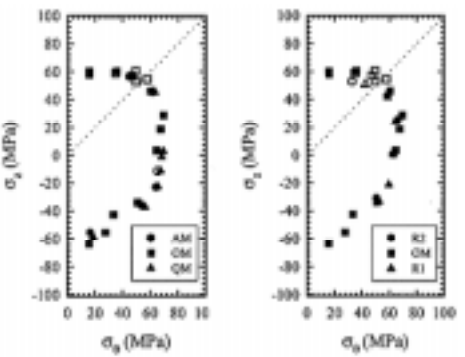

Figure 7. Yield loci shifted to account for residual stress. Dashed line indicates equibiaxial loading. Solid and hollow symbols represent ductile and brittle-type failures, respectively.

CONCLUSIONS

It has been observed that processing conditions are an important factor in the failure mode of aliphatic polyketone. While processing variations yield negligible changes in percent crystallinity or crystalline orientation of the material, it has been determined to affect the ductile/brittle transition through the creation of residual hoop stresses within the samples. While the residual stress accounts for the observed ductile-like behavior under equibiaxial tension, it does not account for the larger range of the brittle-like regime of the annealed sample. Further work is necessary in order to explain this observation.

ACKNOWLEDGEMENTS

The authors gratefully acknowledge Shell Chemical Company for the material and financial support. In particular, the authors would like to thank Dr. C. C. (James) Kau and Dr. Piero Puccini for helpful discussions.

REFERENCES

1 Ash, C., *International Journal of Polymeric Materials*, **30**:1 1-13 (1994).
2 Ash, C. E. and Flood, J. E., *Polymeric Materials: Science and Engineering*, **76** 110-111 (1997).
3 Garbassi, F. and Sommazzi, A., *Polymer News*, **20**:7 201-205 (1994).
4 Kelley, J. W., Roane, D. R. and Le, D. M., 53rd ANTEC 3819 (1995).
5 Karttunen, N. R. and Lesser, A. J., *Journal of Materials Science*, submitted.
6 Lommerts, B. J., Klop, E. A. and Aerts, J., *Journal of Polymer Science: Part B: Polymer Physics*, **31** 1319-1330 (1993).
7 Williams, J. G. and Hodgkinson, J. M., *Polymer Engineering and Science*, **16**:12, 785-791 (1976).
8 So, P. and Broutman, L. J., *Polymer Engineering and Science*, **21**:113, 822-828 (1981).
9 Clutton, E. Q. and Williams, J. G., *Polymer Engineering and Science*, **35** 1381 (1995).
10 Holt, G. A. and Spruiell, J. E., *Polymeric Materials: Science and Engineering*, **76** 112 (1997).

Orientation Effects on the Weldability of Polypropylene Strapping Tape

MJ Oliveira
Dept Eng Polímeros, Universidade do Minho, 4800 Guimarães, Portugal
DA Hemsley
Polymer Microscopy Services, 52 Springfield Close, Loughborough LE 12 5AN, UK

INTRODUCTION

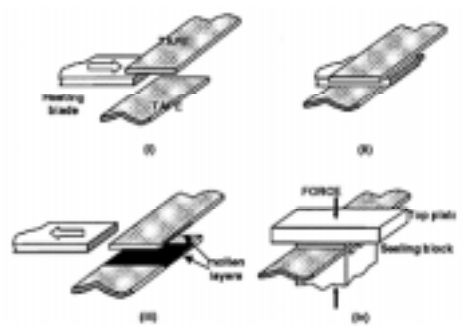

Figure1. Welding sequence.

Polypropylene tape with high tensile strength is commonly used for strapping many products ranging from light cardboard packs to heavy loads such as pallets of bricks or bundles of pipes. It is produced by extrusion followed by drawing at moderate temperatures to achieve high molecular orientation. For reducing fibrillation and to improve the weldability, the tape is embossed after the drawing stage by means of textured hot rolls.

The strapping cycle comprises feeding, tensioning and sealing of the tape around the pack. Thermal welding is the more common sealing process of polypropylene tape, replacing the traditional steel stapling. The welding process involves four steps (Figure 1):

i the heater blade moves in to between the tapes
ii the sealing block moves upwards slightly pressing both surfaces against the blade
iii after a fixed heating time the heater blade retracts
iv the sealing block moves to squeeze the melted surfaces together and cut the unused tape. After a cooling period the welded strap is released.

The production of a strong weld is critical for a good performance of the strap. In this study polypropylene tapes, produced with different draw ratios or having different types of embossing patterns, were welded with a strapping machine. The effect of the welding tem-

perature and the surface profile of the sealing block on the morphology and failure behavior will be presented.

EXPERIMENTAL

This study was carried out on polypropylene strapping tape, of cross-dimensions of 12 x 0.6 mm, supplied by Gerrard Industries (U.K.).

All the tapes were produced from polypropylene homopolymer of MFI about 4 g/600 s (230ºC, 21.6 N). The identification of the tapes is shown in Table 1. It was known that the tapes T_5 to T_9 were drawn in a oven at 95ºC at draw ratios of 5:1 to 9:1, as is indicated by the subscript. A sample of the extrudate from which the tapes were drawn was included in the testing program. Tape T_S, of unknown draw ratio, was included in this study due to the interest in studying a tape with a different type of embossing.

Table 1. Properties of the tapes

Sample indentity	Density, kg m^{-3}	Birefringence $x10^3$	Shrinkage, %	
			130ºC	150ºC
T_5	902	28	7.4±0.5	32±1.5
T_6	902	30	11.0±1.0	34±2.5
T_7	901	36	12.6±0.5	38±3
T_8	901	34	15.8±0.5	39±1
T_9	889	36	16.3±0.5	41±1
T_S	905	28	9.4±0.5	28±1

The following tests and equipments were used to characterize the tapes:

- density measurement by the column gradient method;
- microscopical observation and birefringence measurement, in cross-sections cut along the drawing direction, with a Zeiss Universal polarizing microscope, equipped with a Ehringhaus quartz compensator;
- scanning electron microscopy to observe the embossed surface, using a Leica S 360;
- determination of the shrinkage on annealing at 130ºC and 150ºC in an air circulating temperature controlled oven;
- determination of the tensile strength and elongation at break using a JJ type T 5002 tensile testing machine at a rate of 200 mm/min. The effective cross- sectional area of the

tape was evaluated taking into account the weight and the density of a precisely measured length of tape

The tapes were welded using a semi-automatic Gerrard SA 600–1Z strapping machine at temperatures between 340ºC and 490ºC at 30ºC intervals. The complete welding cycle was 1.4 s. These welds were made using the sealing block with a serrated profile provided with the machine.

For investigating the effect of the block profile and welding pressure some welds were produced with tape T_S at 400ºC with a flat block and a block of higher height, respectively. The effect of misalignment on the strength of the seal was analyzed on tapes welded at 400ºC by imposing to the tape ends the maximum misalignment allowed by the machine (~2 mm).

The microstructure and the mechanical behavior of the welds were studied by means of microscopy and by shear and peel testing.

RESULTS

PROPERTIES OF THE TAPES

The Tables 1 and 2 include the results of the measurements performed on the tapes. The density and the birefringence of the undrawn extrudate was 905 kg m^{-3} and $3x10^{-3}$, respectively.

Table 2 – Mechanical properties of the tapes

Sample	Break load, N	Break strength, MPa	Elongation at break, %
T_5	1509±35	241±6	45±2
T_6	1974±38	315±6	40±1
T_7	1761±48	368±10	34±1
T_8	2395±81	398±13	32±2
T_9	2367±49	406±8	31±1
T_S	1447±47	349±11	40±2

The effect of the draw ratio on the birefringence is shown in Figure 2. The birefringence of the extrudate is very low, compared to that of the tapes, evidencing the strong effect of the drawing operation on the molecular orientation. The increase in birefringence with the draw ratio is sharper for the lower draw ratios. Above the draw ratio of 8:1 the bire-

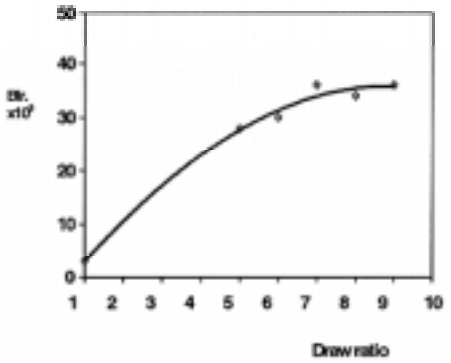

Figure 2. Effect of the draw ratio on the birefringence of the tapes.

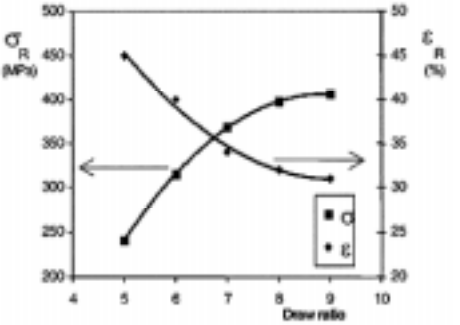

Figure 3. Effect of the draw ratio on the mechanical properties of the tapes.

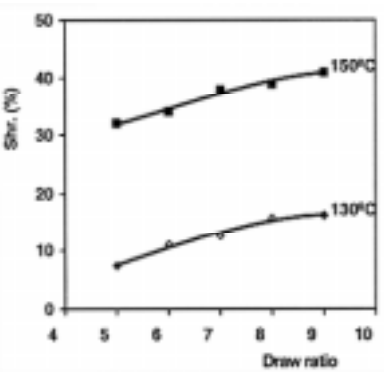

Figure 4. Variation of shrinkage with draw ratio.

fringence tends to level off. Similar behavior was observed by Fransen et al.[1] in polypropylene tapes and by Pezzuti et al.[2] in polyethylene films.

It can be observed in the Figure 3 that the tensile strength of the tapes increases steadily with the draw ratio up to the value of 8:1 and then begins to level off similarly the birefringence behavior. The strain at break decreases with the draw ratio displaying a pattern that is nearly a mirror image of the tensile strength *vs.* draw ratio curve. An identical behavior was observed by Ram et al.[3] in polypropylene tapes. The accentuated decrease in density shown by tape T_9 was certainly caused by voiding and splitting within the structure, suggesting that the improvement in strength by increasing the draw ratio is reaching a limit. As was shown by Mahajan[4] for HDPE tapes drawn at 95ºC and 120ºC those defects increase with draw ratio and with the decrease of the drawing temperature. As it is shown in Figure 4, the shrinkage increases with draw ratio. The values obtained at 150ºC are particularly relevant, from the user's point of view, as they indicate the tendency of the tape to contract near the weld zone. The high shrinkage shown by the tapes at this temperature, between 32 and 41%, suggests that the depth of the heated zone must be kept to a minimum and the tape ends tightly gripped to avoid spoiling the seal by retraction at the welding stage.

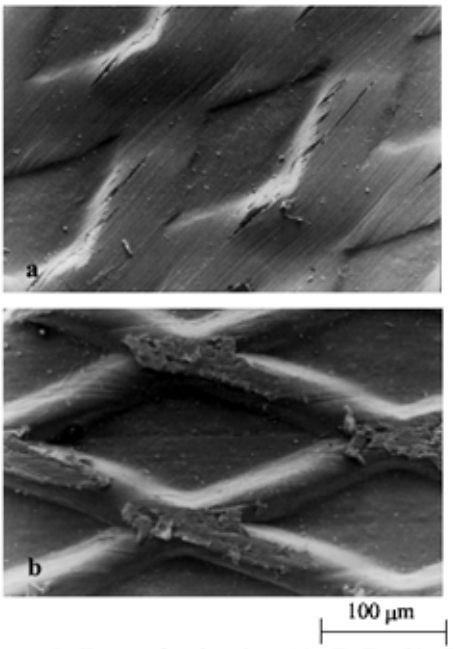

Figure 5.Types of embossing: (a) - T_5-T_9, (b) - T_S.

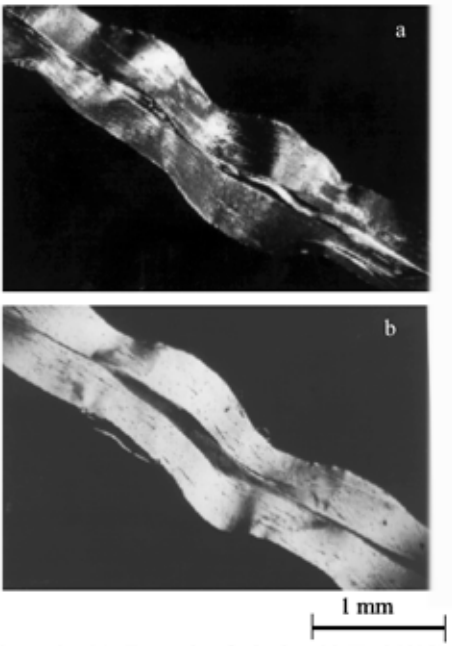

Figure 6. (a) -Example of a bad weld (T_S-340ºC). (b) - Example of a good weld (T_S-370ºC).

The Figure 5 shows the two types of embossing patterns of the tapes. The embossing pattern of tape T_S is deeper and has sharper corners than in the other tapes. The embossing induced splitting of the tapes, this being more severe in the tapes drawn at higher ratios.

WELDING BEHAVIOR OF THE TAPES

The welding temperature has a marked effect on the morphology, strength and failure behavior of the welds. When the heating tool temperature is too low (below 400ºC for most of the tapes) the welds show voids and splits at the interface with the unmelted material. As is illustrated in Figure 6-a, the low temperature and scarcity of the melt prevented the complete filling of the gaps between the matting surfaces resulting in a poor weld. The welds made on tape T_S showed higher splitting than the others for identical welding temperatures. This behavior is certainly caused by the deeper embossing of this tape that demands a higher amount of melt to fill the gaps at the weld zone.

The joints welded at too low temperatures showed low strength (Figure 8) and elongation at break. Depending on the type and amount of defects, the welds broke either at the

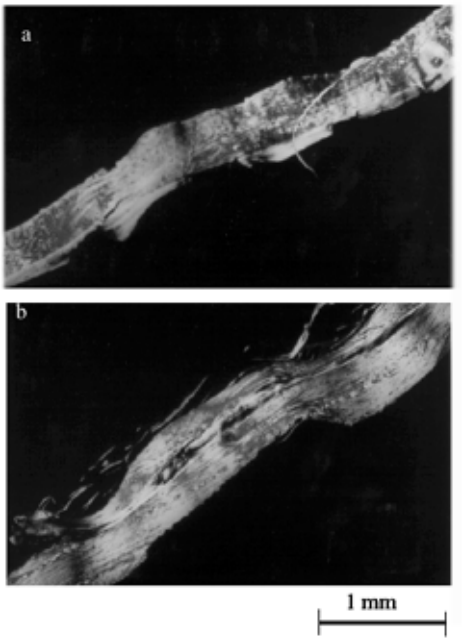

Figure 7. Typical fracture paths of a good weld (T_S – 370ºC). (a) shear test; (b) peel test.

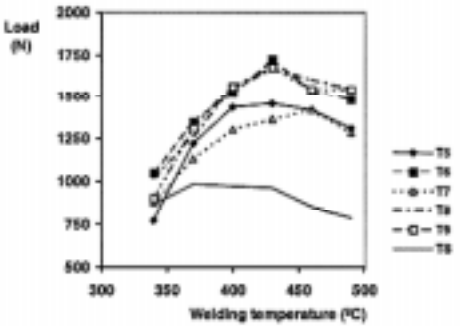

Figure 8. Effect of the welding temperature on the breaking load under shear testing.

seam or at the interface with the unmelted material.

The increase in welding temperature up to 430ºC or 460ºC in the case of tape T_7 resulted in a reduction of the flaws and increase in the shear strength and ductility of the welds. Flow lines and swirls were observed at the widest regions, while at the thinner zones the material oriented in the axial direction of the tape. Figure 6-b shows a typical cross section. Most the welds showed the maximum strength and ductility for a welding temperature of 430ºC (Figure 8). A typical failure of these welds is shown in Figure 7-a. The fracture path runs alternately on both sides of the boundaries of the weld zone, evidencing that the adhesion at the mating surfaces was stronger than at interface with the basic material.

The excessive heating of the tapes, by using tool temperatures of 460ºC or higher changed the morphology and failure behavior of the weld and reduced its strength (Figure 8). The microstructure, that was too fine to be resolved by optical microscopy in the previously referred welds became spherulitic for some tapes and occasionally showed cracks at the mating layer. These cracks probably resulted from a combined effect of degradation of the polymer by excessive heating and increasing contraction upon cooling of the spherulitic structure. The failure generally started at one of the weld ends and moved soon to the basic material.

The peel tests were less effective in assessing the quality of the welds than the shear tests. Above an optimum temperature the peel strength is almost unaffected by the welding temperature. These results correlate well with the failure behavior of the welds under this test. Except in the case of the samples welded at the lowest temperature that fractured through the joint interface, all the others failed through the original material (Figure 7-b). This may be explained by the reduced interfibrillar strength arising from the high molecular orientation of the tape, which made it more susceptible to crack propagation than the unoriented material of the weld.

The modifications made on the surface pattern of the pressing block, namely the flattening of the surface and the increase in the height to increase the welding pressure caused some modifications on the weld morphology. However it only had a marginal effect on the shear strength. The use of the flat block in the tape with deeper embossing caused the welds to be more uniform and this seems to reduce the dispersion of the results.

As expected the misalignment of the tape ends reduced the shear strength of the joint. In the case of the machine used, the maximum misalignment caused a reduction in strength of 4%.

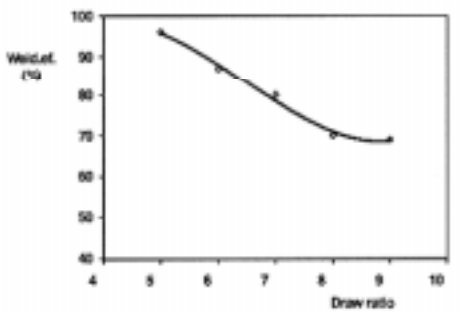

Figure 9. Effect of the draw ratio on the maximum efficiency of the tapes.

The draw ratio of the tapes appears to influence its welding behavior. The tapes with higher orientation (T_7 - T_9) produced thinner welds and with more splits and voids than the less oriented samples. The increase in orientation increases the melting temperature.[5] However for the range of draw ratios used here the difference in melting temperature that could be expected is not enough to explain the reduction in thickness observed. The increase in stiffness with the draw ratio certainly favored the squeezing of the melt out of the weld region, and is probably the main cause of the reduction in thickness observed. The high shrinkage coupled with the high stiffness of the more oriented tapes is also probably the cause of the higher incidence of voids at the weld zone.

The joint efficiency, defined as the ratio between the forces to break the welded and unwelded tape, decreases with the draw ratio up to the draw ratio of 8:1 (Figure 9). Thus, the improvement in strength achieved by drawing the tapes at higher ratios is lost on welding.

CONCLUSIONS

The study carried out in polypropylene tapes with different draw ratios to investigate its welding behavior allowed to draw the following conclusions:

1. The welding temperature has a strong influence on properties of the welds. An optimum welding tool temperature around 430ºC could be defined for most of the tapes.

2. The microstructure of the welds is in general very fine and shows a much lower orientation than the tapes. Welding temperatures of 460ºC or higher produce coarser textures and favor the occurrence of voids and splits at the joints.

3. The welding temperature influences the fracture path of the welds. Below the optimum temperature it runs along one of the interfaces, at the optimum range it alternates between the two interfaces and above the optimum temperature generally moves away from the weld zone.

4. The orientation of the tapes influences the morphology of the welds. The increase in orientation reduces the thickness of the weld zone and favors the formation of voids.

5. The welding efficiency decreases with increasing the orientation of the tapes.

ACKNOWLEDGEMENTS

The authors express their appreciation to Gerrard Industries for supplying the samples and lending the equipment.

REFERENCES

1 P. J. Franssen, J. M. A. Jansen and B. C. Roest, Polypropylene Fibres and Textiles, 2nd Int. Conf. Plast. and Rubber Inst., London, 26-28, Sept., 1979.
2 J. L. Pezzuti and R. S. Porter, *J. App. Polym. Sci*., **30**, 4251-4259, 1985.
3 A. Ram, J. Soker and J. Adorian, *Plast. Rubb. Proc. Appl*., **1**, 363-368, 1981.
4 S. J. Mahajan, B. L. Deopura and Y. Wang, *J. Appl. Polym. Sci*., 60, 1539-1549, 1996.
5 A. O. Ibhadon, *J. App. Polym. Sci*., **43**, 567-571, 1991.

Joint Performance of Mechanical Fasteners under Dynamic Load - Self-Tapping Screws in Comparison with Threaded Inserts in Brass and Plastic

Axel Tome; Gottfried W. Ehrenstein
Institute of Polymer Technology, Univ. Erlangen, Am Weichselgarten 9, 91058 Erlangen, Germany
Frank Dratschmidt
EJOT GmbH&Co KG, Bad Berleburg, Germany

INTRODUCTION

The use of thermoplastic components subjected to dynamic loads and at elevated temperatures becomes more common. The application of glass fiber reinforced plastics for highly loaded parts, e.g. automotive injection molded under-the-hood applications, require an overall knowledge of the joining properties.[1] For low loads, snap-fit joints are especially economic. In case of higher loaded plastic parts, threaded inserts or self-tapping screws can be used for transferring high forces.

This paper compares experimental results of the joint performance between self-tapping screws and both brass and plastic inserts subjected to static and dynamic loading conditions. In particular, the static and dynamic load limits will be discussed.

JOINTS WITH THREADED INSERTS

For joints involving threaded inserts, an insert with an internal thread is placed within one of the parts to be joined, thereby enabling the other part to be screwed onto it with standard screws. Insert joints are used for parts that are subjected to special requirements or for purposes of facilitating assembly and maintenance. Beside standard threaded inserts in metal, which are generally assembled into the component by the hot-embedding or ultrasonic-embedding methods, threaded inserts made of glass-fibre reinforced plastics, which matrix matched to the component, have been on the market for some time for use with the ultrasonic-embedding process. These have considerably shorter acoustic irradiation times and to not need to be removed from the component for recycling.

JOINTS WITH SELF-TAPPING SCREWS

For screw joints with self-tapping screws, a boss with a molded or drilled pilot hole is needed. The screw itself forms the thread during assembly. Self-tapping screws reduce molding and assembly costs by elimination the need for molded threads or secondary tapping operations as necessary for thread inserts. If unlimited repeat assembly is not required, special screws designed for plastic allow for a limited number of disassembly/reassembly cycles. Ten or more reassembly cycles with no deterioration in the joining properties are often possible. The clamp force/prestress force and back out torque are time dependent at a rate that is dependent on the stress relaxation characteristics of the thermoplastic boss material.[2]

JOINT DESIGN

The design methods and dimensioning guidelines of such joints are based on static load tests usually at ambient temperatures.[3-6] Besides dynamic loading,[7-9] the joint is additionally exposed to temperature effects. Temperatures above 80°C up to 150°C in applications under-the-hood are common. Often the temperature is not only static, but superposed by temperature cycles. The prestress force of joints with self threading joints, which determines the quality the joint, are affected by elevated temperatures and temperature cycles.[2]

Earlier investigation show that the boss design can be calculated approximately.[3-6] In practice, the theoretical analysis provides a starting point for design. For fine-tuning of design parameters such as the optimum pilot hole diameter, screw/insert engagement length and boss wall thickness according to the screw/insert-plastic combination require the necessity of experimental investigations.

EXPERIMENTAL

MATERIALS AND SPECIMEN PREPARATION

Glass fiber reinforced polyamide/nylon 6 with 30 wt% short glass fibers (PA6-GF30, Durethan® BKV 30H, BAYER AG) are used for injection molded boss test specimens. The boss geometry was kept constant (wall thickness: 4.5 mm; boss length: 26 mm; pilot hole diameter 4.0 mm) except for the pilot hole diameter for the threaded inserts which was reamed to 5.8 mm respectively up to 8.5 mm according to the insert, Figure 1a. All boss specimens for self-tapping screws had a lead-in section with a diameter of the normal screw (5.0 mm) to a depth of 2.0 mm. The moisture content of the polyamide specimen was about 1.5±0.2 wt%.

Figure 1b shows the design parameter of the boss specimen and the metal screws, which are specially designed for the use with plastics. Both screws have a single lead thread without a cutting slot, a wide thread spacing ($P \approx 0.44 \cdot d$), small core diameters ($d_{core} \approx$

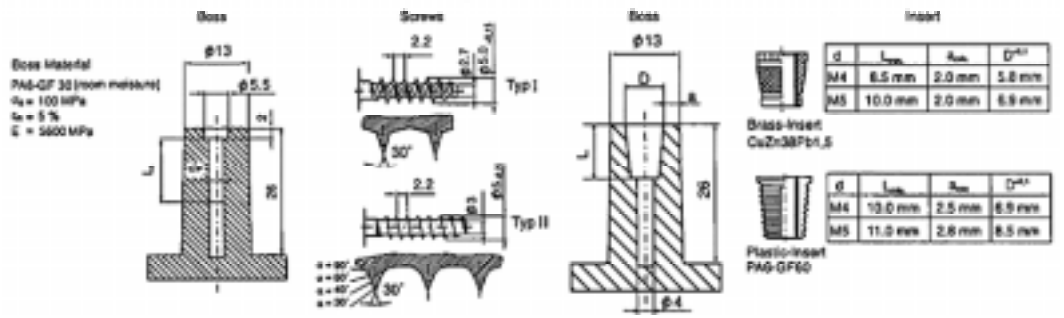

Figure 1. Configuration of thermoplastic boss metallic and plastic inserts (a, right) and self-threading screws (b, left)

0.54·d, d = normal screw diameter) and small thread angles (α = 30°) (manufactured by EJOT/Germany and RIBE/ Germany).

Beside self-tapping screws, standard commercial hot-embedded threaded brass-inserts and ultrasonic-embedded plastic-inserts in sizes M4 and M5 (manufactured by Böllhoff/ Germany) were examined. The plastic insert were made of semi-aromatic copolymer based on PA6-GF60 (Grivory® GV 6H, EMS Chemie).

TEST PROCEDURES

During insertion of the screw, interesting aspects include the torque profile and the prestress force when tightening the screw. In order to measure these values, a screw rig is used that enables the screw assembly to be carried out at continuously adjustable speeds up to 2000 min^{-1}. During assembly, the number of revolutions are constant. The characteristic measurement values (torque, prestress force, screw engagement length, turn angle) are measured continuously. Evaluation is carried out by a linked computer system.

The metallic inserts were hot-embedded the plastic inserts ultrasonic-embedded with the parameters listed in Table 1.

Table 1. Embedding parameters for the insert joints studied

Ultrasonic-embedding (plastic-inserts)		**Hot-embedding (metallic-inserts)**	
Frequency	20 kHz	Temperature	240 to 260^{o}C
Insertion time	0.2 to 0.5 s	Insertion time	1 to 2 s
Holding time	0.3 to 0.5 s	Holding time	2 to 7 s
Pressure	cylinder diameter 50: 1 to 2 bar	Pressure	6 bar

The axial/pull-out strength under quasi-static loading was measured in the short-time pull-out test. To assess the anchoring strength under dynamic load, it is possible to make use of the highly sensitive and precise hysteresis measuring method which has been successfully used for material testing with plastic.[7]

Based on static load tensile tests, force controlled dynamic tensile swell tests were conducted using a Schenk servo-hydraulic testing machine in a load controlled manner. The applied waveform was sinusoidal at a constant minimum-to-maximum load ratio ($R = F_u/F_o$) of 0.1. The test frequency was 5 Hz. Tests were performed at 23°C and 50% relative humidity. The characteristic values were measured according to the hysteresis measurement method. This method is described in several publications (e.g. 6,7).

Hysteresis measurements allow for the simultaneous determination of four different properties during the dynamic test: forces (stresses), displacement (extensions), stiffness and mechanical energy. In addition, the damping factor is calculated from the stored energy and the energy loss, for both linear and non-linear viscoelastic behavior.

Two different loading principles were used in the fatigue test. Stepwise load increased experiments reveal significant value changes and allow the determination of limits for cyclic loading. Then single load level tests prove the correctness of these limits.

RESULTS AND DISCUSSION

STATIC LOAD LIMITS

The determining factor for the strength behavior of insert joints are the shear stress that develops at the interface between the insert and the plastic, or between the screw flank and the insert (also for self-tapping screws) as well as the strength of the joint to the component (failure mode boss fracture). The axial pull-out force of brass-insert, plastic-insert and self-tapping screw joints are shown in Figure 2. For insert joints size M5 the axial pull-out force is comparable to self-tapping screw joints with a screw diameter d_l = 5 mm, however only for a reduced screw engagement length of l_E = 8 mm (standard design: $l_E = 2d_l$ = 10 mm).

DYNAMIC LOAD LIMITS

Figure 3 shows the dynamic characteristic values of brass-insert, plastic-insert and self-tapping screw joint in the stepwise load increased dynamic loading test. These are measured results for individual component joints which are subjected to statistical fluctuations with respect to the maximum upper load (see error bar in Figure 4). The loading force is shown at the top left (controlled value), displaying the curves for upper, F_o, middle, F_m, and lower, F_u, load plotted over the number of cycles. Starting at 0.4 kN the upper load was increased by 0.2 kN after every 5,000 cycles. Prior to each increase, the joint was unloaded and

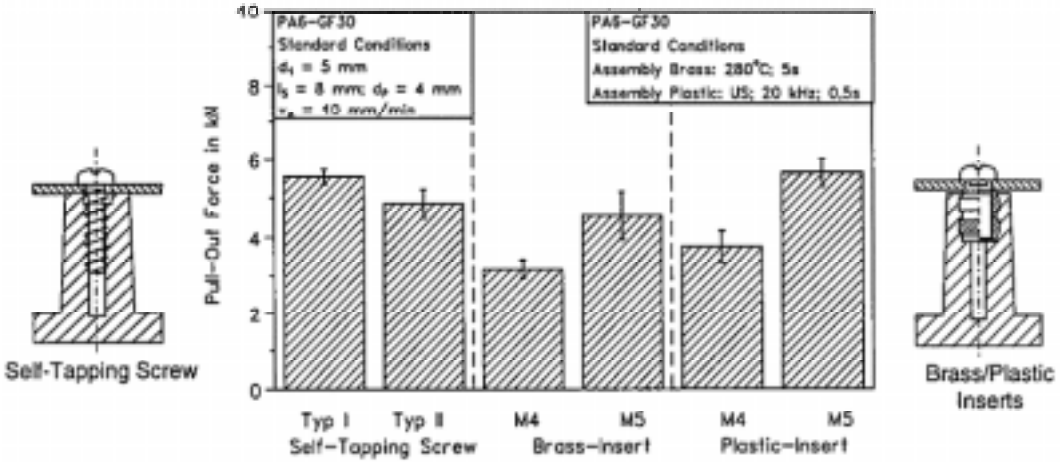

Figure 2. Axial pull-out force of self-tapping screws ($\varnothing$ 5 mm) in comparison with hot-embedded metallic inserts (size M4/ M5) and ultrasonic-embedded plastic inserts (size M4/M5) in PA6-GF30 (23°C/50% RH).[4]

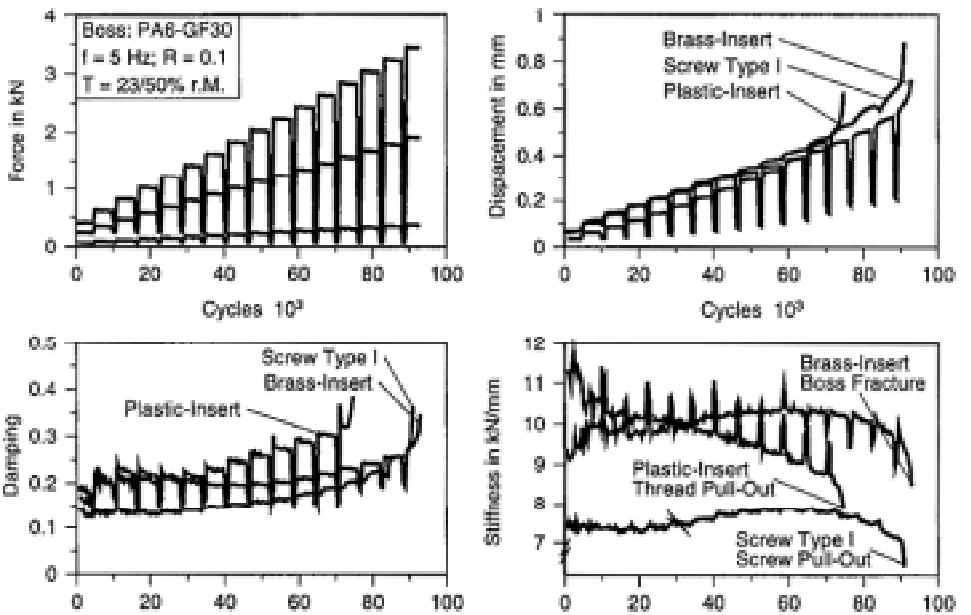

Figure 3. Stepwise load increased dynamic loading of plastic and brass inserts (with force unloading at the end of each level) as well as self-tapping screw (type I) (without force unloading at the end of each level) in PA6-GF30 (23°C/50% RH)

returned to the damage-free basic load level that had prevailed at the start of the test. This

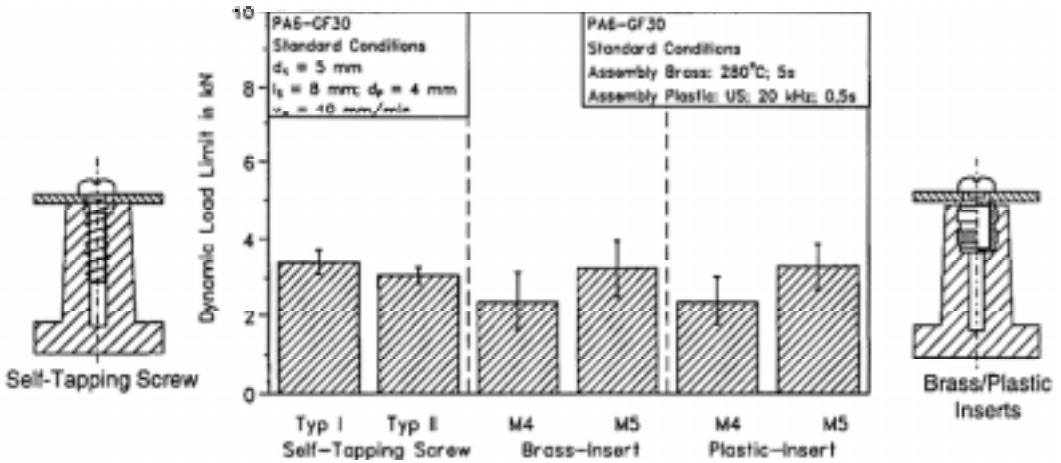

Figure 4. Dynamic load limits of self-tapping screws (∅ 5 mm) in comparison to hot-embedded metallic inserts (M4/M5) and ultrasonic-embedded plastic inserts (M4/M5) in PA6-GF30 (23°C/50% RH).

unloading was only done with insert joints.

The displacement (top right graph) of the joint undergoes a sudden jump when the load is increased, with the plastic-insert and self-tapping screw displaying a slightly higher spontaneous displacement at the start of the test. During the initial load steps, the system displays a linear viscoelastic behavior, since the displacement increases in proportion to the load.

After approximately 50,000 cycles, i.e., as of an upper load of 2.0 kN, a more pronounced increase in displacement is observed for both the insert joint as well as the self-tapping screw joint. This would indicate a greater level of creep and hence an increase in the non-linear viscoelastic deformation, which is irreversible. In the current example, failure occurs in the brass-insert joint at approximately 75,000 cycles, i.e., with the load increase to 3.0 kN, through the boss tearing off. This is shown by the sharp increase in the displacement. The plastic insert and self-tapping screw joint failed after approximately 95,000 cycles (3.4 kN), i.e., through thread pull-out/shear-off or rather screw pull-out (self-tapping screw).

The highly unproportional increase in damping and displacement that occurs with each load increase, together with the unproportional decrease in the stiffness above 30,000 cycles (brass-insert), i.e. 1.6 kN respectively above 50,000 cycles (plastic-insert/self-tapping screw), i.e. 2.0 kN, points to increasing non-elastic deformation or to potential damage development. The increasing rise in the damping, with a continuous reduction in the stiff-

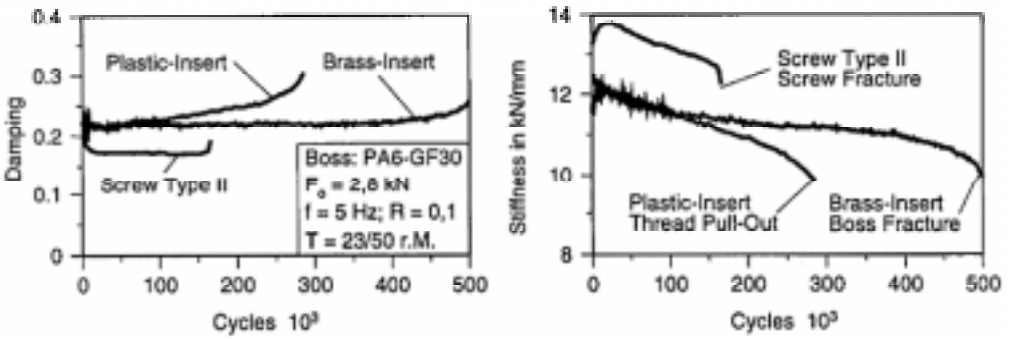

Figure 5. Single load level experiment (F_o = 2.8 kN) with joints in PA6-GF30.

ness of the brass-insert at the same time, shows that initial damage to the joint and probably cracking occurs after 30,000 cycles already, which ultimately leads to the boss fracture after 75,000 cycles (3.0 kN). The dynamic load limits of the brass-insert, plastic-insert and self-tapping screw are summarized in Figure 4. Under dynamic load, the pull-out strength decreases for PA6-GF30 to approximately 60% of the pull-out strength of plastic-inserts and self-tapping screw for quasi-static loading and to approximately 70% of this value for brass-inserts.

Figure 5 shows results from the single-step fatigue test with an upper load of 2.8 kN. The upper loads are in the range of the failure loads established in the load-increase test. While the brass-insert only displays a unproportional increase in the dynamic characteristics values above 480,000 cycles, and fails through boss fracture at approximately 500,000 cycles, the plastic insert fails above 250,000 cycles through thread pull-out/ shear-off. The dynamic behavior of the self-tapping screw is limited by screw fracture. Therefore, the interphase screw flank/plastic does not determine the dynamic load limit, but the endurance-limit of the metallic screw depends on the small core diameter.

With an reduction of the upper load, the dynamic long-time behavior increases to larger cycles. Figure 6 shows joints after 10^6 cycles without rupture by an upper load of 2.0 kN (single load level experiment). For self-tapping screws and plastic-inserts no cracks are evident. At the runout of the brass-insert (here: size M4) notch effects cause cracks to develop, which was evident by with an increase in damping after 700,000 cycles. The decisive factor is that, even on fatigue specimen that has not ruptured, it is possible to observe cracks. This would suggest that the fatigue strength had not been attained, with this upper load at least, considering the characteristic values for stiffness and damping and microscopic studies.

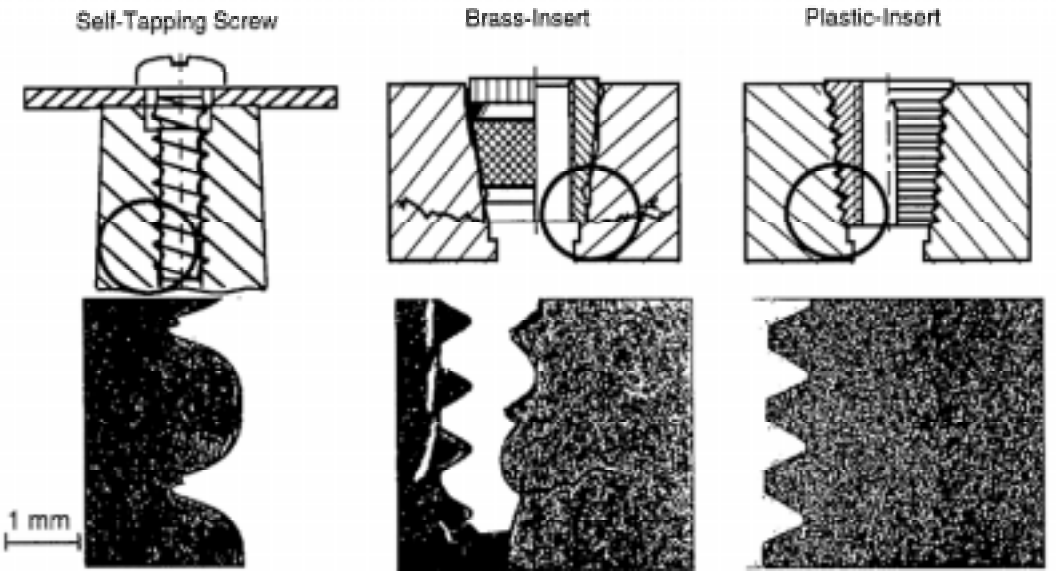

Figure 6. Joints after 10” cycles without rupture with an upper load of 2.0 kN. For self-tapping screw and plastic inserts in opposite to brass-insert, no cracks are evident. The cracking at the runout of brass-insert was evident with an increase in damping after 700,000 cycles.

CONCLUSIONS

The static pull-out limit of joints with brass-inserts (size M5) is comparable to joints with plastic-inserts (size M5) as well as self-tapping screws (∅ 5 mm), e.g. in PA6-GF30. The joint fail via pull-out of the insert or self-tapping screw.

The dynamic load limit measured in the stepwise dynamic load increase test of self-tapping screw and plastic insert is about 3.4 kN, and brass-inserts about 3.0 kN. The joint failures via boss fracture (brass-insert), thread pull-out/shear-off (plastic-insert) and screw pull-out (stepwise load increase test) or screw fracture (single load test). In opposite to joints with self-tapping screws or plastic inserts, cracks can be observed in microscopic studies at joints with brass-inserts, e.g. even on fatigue specimen that have not ruptured after 10^6 cycles. An estimate of the upper load for durable load transformation in the plastic component is not possible at present on the basis of the measured results that have been obtained. It is, in fact, doubtful whether a fatigue strength range can be given at all in view of the notch effects.

The advantage of joints with brass-inserts is the limited relaxation of the clamp/prestress force, e.g. by fixing the metallic component on the brass-insert. In every case in which the plastic component is fixed, the clamp/prestress force will be reduced by the time

dependent relaxation. In this paper we have not discussed this effects for joints with self-tapping screws and plastic-inserts.

ACKNOWLEDGEMENTS

The authors would like to thank the screw producing companies Ribe and EJOT, Germany, which supported these investigations. BAYER AG, Germany, is gratefully acknowledged for material support.

REFERENCES

1 Smock, D. (1994), „Plastics move under the hood“, *Design News*, 10 pp. 148-152.
2 Tome, A. and Ehrenstein, G.W. (1999), „Time dependent prestress force of threaded joints. Antec 99, pp. 1327-1331.
3 Onasch, J. (1982), "Zum Verschrauben von Bauteilen aus Polymerwerkstoffen mit gewindeformenden Metallschrauben"; Ph. D. Thesis, University of Kassel.
4 Ehrenstein, G.W. (1995), "**Mit Kunststoffen konstruieren**", Munich, *Carl Hanser Verlag.*
5 Onasch, J. and Ehrenstein, G.W. (1982), "Calculation methods for the joining of plastic parts by thread-forming screws", Translated from *Kunststoffe*, **11**, pp. 720-724.
6 Großberndt, H. and co-authors (1988), „**Die automatische Schraubenmontage**“, Ehningen, *Expert Verlag*.
7 Dratschmidt, F. and Ehrenstein, G.W. (1997), "Threaded Joints in Glass Fiber Reinforced Polyamide", *J. Polym. Eng. Sci.*, Vol. **37**/4 pp. 744-755.
8 Dratschmidt, F. (1999), "Zur Verbindungstechnik von glasfaserverstärktem Polyamid", Ph. D. Thesis, Institut for Polymer Techmology, Uni Erlangen/Germany.
9 Tome, A., Dratschmidt, F. and Ehrenstein, G.W. (1999), „Threaded Inserts in Plastic“, *Plast Europe* Vol. **89** (5), pp. 16-18.

Defect Cost Analysis

Christoph Roser and David Kazmer
University of Massachusetts Amherst, Amherst, Mass., USA

INTRODUCTION

Engineering design is a complex and sophisticated task in order to create a successful product. One major element of a successful product is to reduce the cost of the product while satisfying the specifications. Specifications are the requirements towards the design responses to satisfy the user requirements. This is done by constraining the design responses. Here the development team has to achieve a trade-off between the satisfaction of the constraints and the cost minimization. However, the constraint satisfaction and the total cost of the design are coupled, because increased quality usually creates increased cost, but also reduces the likelihood of defects. The demonstrated methodology will aid the development team in understanding this coupling in order to minimize the total cost of the product by decomposing the total cost and assigning the cost towards the different cost drivers. Then the development team can analyze what causes the cost of the product and thus improve the design towards a more economic design. This enables the development team to improve the design focused on the actual cost drivers, avoiding the improvement of design responses which do not contribute towards the total cost. However, it has to be taken under consideration that a design performance is driven by other reasons than cost. This value analysis is not discussed in this paper.

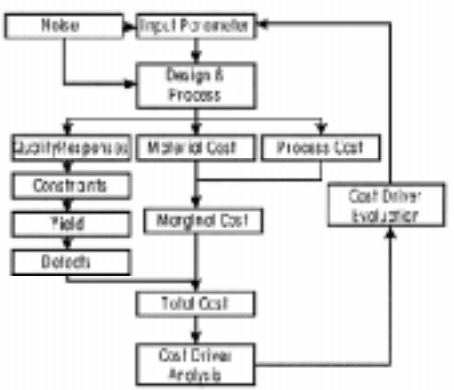

Figure 1. System overview.

SYSTEM OVERVIEW

The engineering design model consists of input parameters, which are determined by the product development team, and output responses, which are a function of the input parameters. Furthermore a design is subject to noise, distorting the input parameters and the resulting output responses. Figure 1 visualizes the system as utilized in this methodology.

The input parameters x_i are applied to the design and the processing of the design, which in turn will determine the output responses y_j. However, as the input parameters of the design and process are subject to noise the output responses will exhibit variation. Therefore, both the input parameters and the output responses are no crisp values but rather a probabilistic distribution. In the following, this distribution is denominated as ϕ. An example for a normal distributed input parameter is given in,[1] where the additional information of the mean and the standard deviation is required.

$$\phi_{x_i} = \frac{1}{\sigma\sqrt{2\pi}} e^{\left(\frac{-(x_i-\mu)^2}{2\sigma^2}\right)} \quad [1]$$

The distribution f of the input factors x_i will determine the distribution f of the responses y_j. It is assumed that the distributions of the constrained responses y_j are independent of each other.

$$\phi_{y_j} = f(\phi_{x_1}, \phi_{x_2}, \phi_{x_3}, \ldots \phi_{x_0}) \quad [2]$$

In this case, the output responses are divided into three groups, which are part of every design. One response is the utilized material cost C_M, including all materials and standard components needed to create a product, including waste material like sheet metal cut offs or injection molding runner material. It does not include secondary supplies like maintenance material for the production process. These costs are included in the second group of processing cost C_P, which also includes machine cost, man-hour cost, amortized tooling, etc. The third and last group contains the cost due to inadequate quality, in which the resulting part properties are compared with the correlated constraints. Examples for this group are the weight, the strength, chemical resistance, and so on. These responses can be constrained in three different ways such that the response has to be below, above or in between a given limit, where *LSL* is the lower specification limit and *USL* is the upper specification limit.

$$\begin{aligned} LSL_j &< y_j \\ y_j &< USL_j \\ LSL_j &< y_j < USL_j \end{aligned} \quad [3]$$

MARGINAL PART COST

The marginal part cost C_{MP} is simply the sum of the material cost and the process cost. It is the cost required to produce one additional quantity of the design.

$$C_{MP} = C_M + C_P \quad [4]$$

YIELD

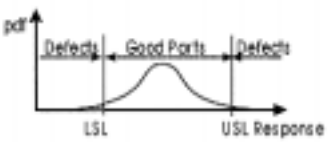

Figure 2. Distributed response.

In this methodology, a good part is defined as a part satisfying all specifications, and a bad part is defined as violating one or more specifications. Due to the stochastic nature of the input variables and the processing, the same input parameter values will not always result in identical output response values but rather a distribution. Therefore, there is a certain possibility of violating a constraint. The probability density function (pdf) of a normal distributed example is given in Figure 2, where the response is bounded by two constraints, with the likelihood of defect parts equal to the shaded areas of the curve outside of the limits and the likelihood of good parts equal to the non shaded area of the curve between the limits. The probability *P* of satisfying one constraint if the response y_j is calculated by integrating the response distribution between the correlated *LSL* and the *USL*.

In case the constraint is one sided then the other side is set to $-\infty$ for the *LSL* or to $+\infty$ for the *USL*.[1] The probability can be evaluated from the evaluation of constraint satisfaction.

$$P_i = \int_{LSL_i}^{USL_i} \phi_{y_i} dy_i \qquad [5]$$

This integration will always yield a value between zero and one inclusively if the distribution ϕ of y_i is a valid probability density function. The joint probability of success for meeting multiple quality requirements, P_{Joint}, is calculated by multiplying the probabilities P of success of each response *y* for all n constrained responses, assuming the independence of the responses y.[2] P_{Joint} represents the percentage yield of acceptable parts.

$$P_{Joint} = \prod_{i=1}^{n} P_i = \prod_{i=1}^{n} \int_{LSL_i}^{USL_i} \phi_{y_i} dy_i \qquad [6]$$

TOTAL COST

After calculating the marginal part cost C_{MP} and the total yield P_{Joint} of the product, the total cost C_T can be calculated. The marginal part cost occurs for every produced part, no matter if the part is defect or acceptable. However, every defect part is rejected, therefore the total cost of the production of one good part also has to include the appropriate cost for the production of the defect parts. Therefore, the total average part cost is calculated as the marginal part cost divided by the yield.

$$C_T = \frac{C_{MP}}{P_{Joint}} = \frac{C_M + C_P}{\prod_{i=1}^{n} \int_{LSL_i}^{USL_i} \phi_{y_i} dy_i} \quad [7]$$

COST DRIVER ANALYSIS

So far, the demonstrated procedure is - although not standard in the industry - rather well known in the research community. However, this paper will now reverse analyze the total cost C_T of the product in order to determine the cost driver in the product. One possible approach would be to determine the cost of all defects and compare it with the cost of all defects excluding the investigated defect. This is similar to the cost change if the probability of constraint satisfaction for the investigated response would be perfect with no change to the other responses. Two cost drivers are already known, the material cost C_M and the process cost C_P. The defect cost is then the remainder towards the total part cost. This cost due to the defects C_D can be calculated by subtracting the marginal part cost C_{MP} from the total cost C_T.

$$C_D = C_T - C_{MP} \quad [8]$$

Now it is possible to compare the defect cost of all defects with the defect cost excluding the analyzed constraint j. The defect cost excluding constraint j, $C_{De\phi j}$, is calculated similar to the defect cost by ignoring the performance requirement y_j.

$$C_{De\phi j} = C_{MP}\left[\frac{1}{\prod_{i=1,\, i\neq j}^{n} \int_{LSL_i}^{USL_i} \phi_{y_i} dy_i}\right] \quad [9]$$

As $C_{De\phi j} \leq C_D$ the decrease in cost C_{Dej} for a optimal constraint satisfaction $P_j = 1$ would be the difference between the defect cost C_D and the defect cost excluding j $C_{De\phi j}$.

$$C_{Dej} = C_D - C_{De\phi j} \quad [10]$$

While this approach is mathematically justified, it has one flaw reducing its understandability and easy to use. As the joint probability of success, P_{Joint} and the resulting total cost depend on all responses, there exists interaction between C_D and C_{Dej}, i.e., a part may be rejected due to multiple defects. Therefore, the sum of all C_{Dej} may exceed the defect cost C_D.

$$C_D \leq \sum_{j=1}^{n} C_{Dej} \qquad [11]$$

Although the methodology is mathematically correct, it may lead to confusion if it is expected that the sum of all single defect costs equal the total defect cost. Similarly, a defect cost can be measured by calculating the expected defect cost if all other qualities are assumed perfect, $P_i = 1$, $i \neq j$, and only the defect probability of response j is taken under consideration.

$$C_{Doj} = C_D - C_{MP}\left[\frac{1}{\int_{LSL_i}^{USL_i} \phi_{y_j} dy_j}\right] \qquad [12]$$

For the same reasons mentioned above, the sum of all single defect costs, C_{Doj}, may be less than the total defect cost C_D.

$$C_D \geq \sum_{j=1}^{n} C_{Doj} \qquad [13]$$

Therefore, the presented methodology of defect cost analysis will evaluate the ratio of a single defect probability with the sum of all defect probabilities. This is done by dividing the probability of failure of one response *i* by the sum of all probabilities of failure, which yields the effect *E* of the response *i* on the total cost, where E_j may range from 0 to 1.

$$E_j = \frac{1 - P_j}{\sum_{i=1}^{n} (1 - P_i)} \qquad [14]$$

This percentage effect E_i of each constraint violation on the cost due to the yield is then simply multiplied with the cost due to the yield C_Y to get the cost due to the violation of a single constraint C_i.

$$C_j = C_Y E_j = C_Y \frac{1 - P_j}{\sum_{i=1}^{n} (1 - P_i)} \qquad [15]$$

The cost effect of each defect and quality specification can be measured monetary. In addition, the sum of all single defect costs equals the total defect cost.

$$C_D = \sum_{i=1}^{n} C_i \qquad [16]$$

If it is assumed that all quality responses are optimized towards a P_i of one as shown in [15] by calculating C_j, then the C_{Dej} will overestimate the defect cost, whereas the C_{Doj} will underestimate the defect cost.

COST DRIVER EVALUATION

As stated in [2], the input variables and the output responses are related. Therefore if the effect of the output responses y are known, it is possible to determine which response is the least satisfying, i.e. the most expensive response. Then it is possible to reverse the relation between the input variables and the response to evaluate the input variables, which can improve the selected response. The goal is to adjust those input variables to minimize the total cost of the product.

EXAMPLE

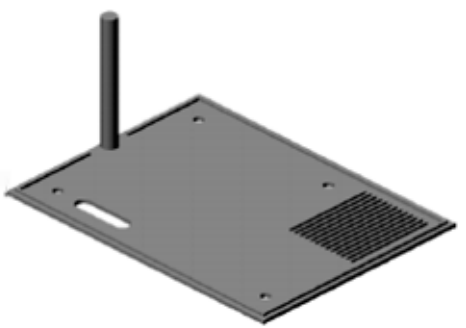

Figure 3. Example part.

The methodology will be demonstrated on an injection molded part as shown in Figure 3.

This part consists of a flat plane with slots and holes, a small protrusion and a runner system. To simplify the relations between the input parameters and the output responses it is assumed that the part shows the behavior of a flat plate of similar dimensions. The investigated input parameters listed below include a material parameter, a design parameter and two process parameters:

- Molecular Weight
- Melt Temperature
- Injection Time
- Thickness

In order to estimate the quality distribution, a standard deviation was estimated for each input from the knowledge of the process characteristics and applied to the input parameter. The underlying relations between the inputs and the responses are known from different models and simulations, including structural analysis, material prediction, and process simulation. These models also included noise and uncertainties as normal distributions were applied to all model parameters and other input parameters not listed above. To achieve dis-

tributed output responses these models and simulations where run repeatedly utilizing design of experiments, with the input variables and model parameters distributed according to the probabilistic density functions of the input parameters. The distribution of the responses was estimated as normal distribution based on the sample data, where m is the number of runs per experiment, l is the numerator for the different runs and i is the numerator for the responses.

$$\mu_{il} = \frac{\sum_{k=1}^{m} y_{ikl}}{m} \forall (i, l) \quad [17]$$

$$\sigma_{il} = \frac{\sum_{k=1}^{m} (y_{ikl} - \mu_{il})^2}{m-1} \forall (i, l) \quad [18]$$

The performance specifications included moldability, cost and design responses.

- Deflection
- Material Cost
- Process Cost
- Cycle Time
- Shear Rate
- Maximum Injection Pressure

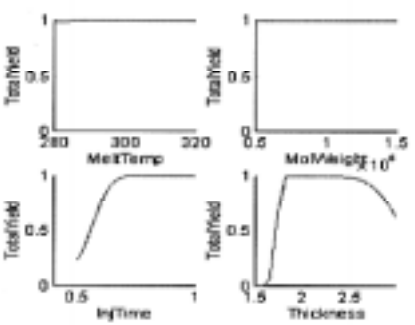

Figure 4. Yield.

Due to the computation time required to calculate the quality responses, a second order response surface was fitted through the data points based on a central composite design of experiments, predicting the mean and the deviation of the output responses.[3] Using this response distribution, the probability of success for one response P_i was determined for each response and subsequent the probability of satisfying all responses P_{joint} was calculated according to [5] and [6].

Figure 4 shows the relations between the input parameters and the yield. It can be seen that the injection time and the thickness have the most significant effect on the yield, as the total yield varies between 0 and 1, whereas the melt temperature and the molecular weight have very little effect on the yield, which is almost constant. Note that the figure shows the rela-

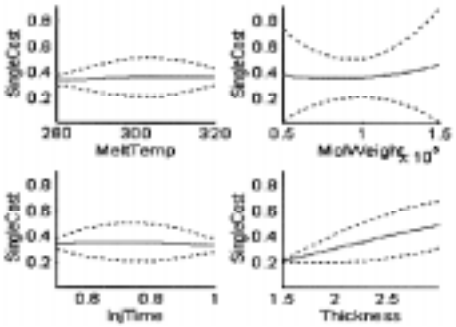

Figure 5. Marginal cost.

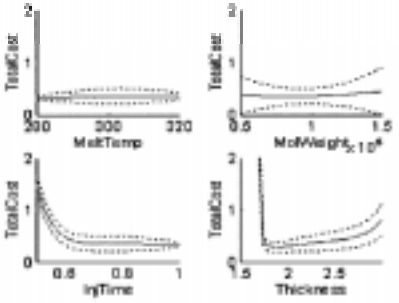

Figure 6. Total cost.

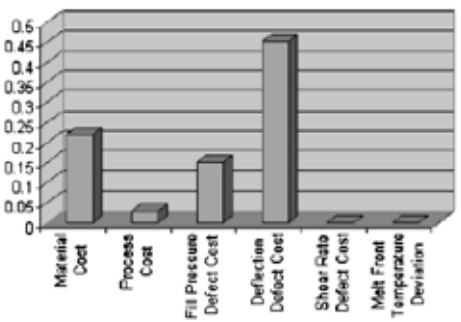

Figure 7. Cost driver.

tions at the midpoint of the design space. The relations change if the graphs are plotted at another point in the design space due to interactions.

Figure 5 shows the relations between the input parameters and the marginal cost, where the centerline is the expected mean and the dashed lines on both sides represent three standard deviations from the mean. The marginal cost was created based on the volume of the part, its production time and the required machine size based on the maximum pressure. As there is large variation in the marginal cost, the mean values are flat and only the thickness of the part shows an effect due to the increase in material consumption and cooling time.

Using [7] the total cost is derived based on the marginal part cost and the yield as shown in Figure 6. It can be seen clearly that the total cost rises if the yield goes down. This graph can be derived from Figure 4 and Figure 5. Note that the total cost increases dramatically if the yield becomes very low.

Using the information from above it is possible to estimate the effect of the various cost drivers towards the total cost using [8] and [15]. This effect is shown in a bar graph in Figure 7 for a sub optimal point in the design space with the following values:

Melt Temperature:	294°C
Molecular Weight:	100,000 mers
Injection Time:	0.6 s

Thickness: 1.7 mm

The total cost of producing one part for the given design space point is \$0.85. The cost drivers for this given design point are

Material Cost: \$0.22
Process Cost: \$0.03
Fill Pressure: \$0.15
Deflection: \$0.45
Shear Rate: \$0.00
Melt Front Temperature: \$0.00

It can be seen that in this case the main cost driver are deflection defects, followed by the material cost and the fill pressure defects. Therefore, significant cost is generated because the product is not stiff enough and is likely to bend or break under the specified load. Applying the relations between the responses and the input parameter, it was determined that the thickness is the main driving input variable for those responses. By increasing the thickness to 1.95 mm, it was possible to reduce the defect cost due to the stiffness and fill pressure to \$0.00, with only a slight increase in material cost to \$0.25 and process cost to \$0.04, minimizing the total cost of the product to \$0.29 and creating a robust designed part.

CONCLUSIONS

The analysis of the cost drivers enables the development team to improve the design by focusing on the most significant contributions toward the cost. This analysis is measured in monetary units, making the results easy to understand and to estimate the impact of the different cost drivers. Future research includes an improved estimation and visualization of the significance of the input parameters towards the cost drivers, enhancing the understanding of the relation between the input parameter and the total cost. It is also intended to implement the shown methodology in a commercially available CAD software package.

NOMENCLATURE

μ	Mean
σ	Standard Deviation
ϕ_x	Distributed Input Parameter
φ_y	Distributed Response
C_D	Cost due to Defects
$C_{De\phi j}$	Cost due to Defects excluding j
C_{Dej}	Cost reduction due to Defects excluding j
C_{Doj}	Cost due to Defects of Response j only

C_i	Cost due to a Single Response
C_M	Material Cost
C_{MP}	Marginal Part Cost
C_P	Process Cost
C_T	Total Cost
E_i	Percentage Effect of Response I
i,j	Counters
k	Sample Counter
l	Experiment Run Counter
LSL	Lower Specification Limit
m	Sample Size
n	Number of Constrained Responses y
o	Number of Input Parameters x
P_i	Probability of Success for one Response
P_{Joint}	Joint Probability of Success
USL	Upper Specification Limit
x_i	Input Parameter
y_i	Output Response

ACKNOWLEDGMENTS

The author would like to thank Stephen Shuler and Don Richwine from GE Plastics. Portions of this work was supported by the National Science Foundation (Grant No. DMI-97-02797).

REFERENCES

1 Devore, J.L. (1995) **Probability and Statistics for Engineering and the Sciences**. *Wadsworth*.
2 Papoulis, A. (1991) **Probability, Random Variables, and Stochastic Processes**. *McGraw-Hill*.
3 Schmidt, S.R., et al. (1994) **Understanding Industrial Designed Experiments**. *Air Academy Press*, Colorado Springs, Colorado.